In Situ and Operando Investigation of the Dynamic Morphological and Phase Changes of Selenium-doped Germanium Electrode during (De)Lithiation Processes

Tianyi Li[1‡], Cheolwoong Lim[1‡], Yi Cui[1], Xinwei Zhou[1,2], Huixiao Kang[1], Bo Yan[1,3], Melissa L. Meyerson[4], Jason A. Weeks[4], Qi Liu[5], Fangmin Guo[5], Ronghui Kou[5], Yuzi Liu[2], Vincent De Andrade[5], Francesco De Carlo[5], Yang Ren[5], Cheng-Jun Sun[5], C. Buddie Mullins[4], Lei Chen[6], Yongzhu Fu[7], and Likun Zhu[1*]

[1]Department of Mechanical and Energy Engineering, Indiana University Purdue University Indianapolis, Indianapolis, IN 46202

[2]Center for Nanoscale Materials, Argonne National Laboratory, 9700 South Cass Avenue, Argonne, Illinois 60439

[3]School of Materials Science and Engineering, Shanghai Jiao Tong University, Shanghai, 200030, China

[4]McKetta Department of Chemical Engineering and Department of Chemistry, University of Texas at Austin, Austin, TX 78712

[5]Advanced Photon Source, Argonne National Laboratory, Argonne, IL 60439

[6]Department of Mechanical Engineering, Mississippi State University, Mississippi State, MS, 39762, USA

[7]College of Chemistry, Zhengzhou University, Zhengzhou 450001, P. R. China

‡ These authors contributed equally to this work

*Corresponding author: likzhu@iupui.edu (L. Zhu)

This is the author's manuscript of the article published in final edited form as:

Li, T., Lim, C., Cui, Y., Zhou, X., Kang, H., Yan, B., Meyerson, M. L., Weeks, J. A., Liu, Q., Guo, F., Kou, R., Liu, Y., Andrade, V. D., Carlo, F. D., Ren, Y., Sun, C.-J., Mullins, C. B., Chen, L., Fu, Y., & Zhu, L. (2020). In situ and operando investigation of the dynamic morphological and phase changes of a selenium-doped germanium electrode during (de)lithiation processes. Journal of Materials Chemistry A, 8(2), 750–759. https://doi.org/10.1039/C9TA09750C

Abstract

To understand the effect of selenium doping on the good cycling performance and rate capability of a $Ge_{0.9}Se_{0.1}$ electrode, the dynamic morphological and phase changes of the $Ge_{0.9}Se_{0.1}$ electrode were investigated by synchrotron-based operando transmission X-ray microscopy (TXM) imaging, X-ray diffraction (XRD), and X-ray absorption spectroscopy (XAS). The TXM results show that the $Ge_{0.9}Se_{0.1}$ particle preserves its original shape after the large volume change induced by the (de)lithiation and undergoes a more sudden morphological and optical density change than pure Ge. The difference between $Ge_{0.9}Se_{0.1}$ and Ge is attributed to a super-ionically conductive Li–Se–Ge network formed inside $Ge_{0.9}Se_{0.1}$ particles, which contributes to fast Li-ion pathways into the particle, nano-structuring of the Ge, as well as buffering the volume change of Ge. The XRD and XAS results confirm the formation of the Li–Se–Ge network and reveal that Li–Se–Ge phase forms during the early stages of lithiation and is an inactive phase. The Li–Se–Ge network also can suppress the formation of the crystalline $Li_{15}Ge_4$ phase. These in situ and operando results reveal the effect of the in situ formed, super-ionically conductive, and inactive network on the cycling performance of Li-ion batteries and shed light on the design of high capacity electrode materials.

Keywords: Li-ion battery, Selenium-doped Germanium, in situ synchrotron transmission X-ray microscopy, operando X-ray diffraction, operando X-ray absorption spectroscopy

1. Introduction

Germanium (Ge) has been considered a promising anode active material for high energy density Li-ion batteries (LIBs)[1, 2], due to its high capacity, low voltage, fast Li diffusion, and high electrical conductivity. Similar to other high capacity anode materials, such as silicon (Si) and tin (Sn), Ge electrodes experience large volume changes (about 337% for full lithiation to $Li_{15}Ge_4$) in the Ge particles during (de)lithiation processes. The repeated large volume change causes particle fracture and electrode delamination from the current collector, thereby leading to rapid loss of specific capacity. Recently, particle fracture has been alleviated by nano-structuring the alloy-type anode materials, such as Ge, Si, and Sn, due to the facile strain accommodation and the short diffusion path for electron and Li transport in these nanostructured materials[3-7]. However, nano-structured particles have not become commercially relevant due to their high cost, solid electrolyte interface (SEI) issue, and difficulty for scale up[8, 9]. Another approach to withstanding massive strain in high capacity anode materials is to design composites containing a high capacity anode material and a stress-accommodating phase[9]. For instance, Klavetter et al. have shown that μm-sized selenium (Se)-doped Ge particles vastly outperform un-doped Ge particles of similar size in their cycling stability and rate capability (Fig. S1)[10]. These results demonstrate the possibility to develop commercially relevant anode materials that can be cast into films with high energy density and cycling stability. It has been hypothesized that the super-ionically conductive inactive phase (Li-Se-Ge) buffers the volumetric change of the active phase (Ge) and increases the rate of Li diffusion during (de)lithiation processes. However, the effect of the active/inactive mixed phases on the mechanical stability of $Ge_{0.9}Se_{0.1}$ electrode is still elusive. The objective of this paper is to investigate the dynamic morphological evolution and crystalline

phase transformations of $Ge_{0.9}Se_{0.1}$ particles during (de)lithiation processes and reveal the effect of the active/inactive mixed phases.

Recently, synchrotron transmission X-ray microscopy (TXM) [11-18], X-ray diffraction (XRD) [19-22], and X-ray absorption spectroscopy (XAS) [19-22] technologies have been utilized to characterize the dynamic morphological and phase changes of high capacity LIB anode materials during (de)lithiation processes. There are several reports which focus on Ge electrodes. For instance, Weker et al. used 44 nm resolution two-dimensional (2D) TXM to observe the volume change and degradation of μm-sized Ge particles during the first two cycles[17]. Lim et al. carried out a combination of operando XRD and XAS to investigate the phase transformations of Ge anodes[22]. They found that crystalline $Li_{15}Ge_4$ is the final lithiation product and the cycling process is between amorphous Ge and crystalline $Li_{15}Ge_4$ after the first cycle. They also studied the effect of cycling rate on Ge phase transformation during the first cycling process. Silberstein et al. studied the phase transformations within Ge nanowires throughout the course of LIB cycling using operando XRD and XAS[21]. They identified more crystalline Li_xGe phases during the cycling process and revealed that amorphous regions within Ge nanowires are preferentially lithiated before crystalline regions.

In this study, we investigated the dynamic morphological change of Ge and $Ge_{0.9}Se_{0.1}$ electrodes during (de)lithiation processes using a combination of 2D operando TXM imaging and 3D in situ TXM tomography. In addition, we carried out operando XRD and XAS to study the dynamic phase transformation of the $Ge_{0.9}Se_{0.1}$ electrode. Synchrotron TXM was implemented for both

Ge and $Ge_{0.9}Se_{0.1}$ electrodes under 11.2 keV X-rays at beamline 32-ID-C of the Advanced Photon Source (APS). In situ 3D tomography with 77.6 nm pixel size was implemented at three electrode states in the first cycle: pristine, lithiated, and delithiated, and operando 2D imaging with 38.8 nm resolution was implemented between those three conditions. The operando XRD experiment was conducted at beamline 11-ID-C of the APS and the operando XAS experiment was conducted at beamline 20-BM of the APS. With the in situ and operando results, the morphological and phase evolutions of Ge and $Ge_{0.9}Se_{0.1}$ electrodes were analyzed and compared. The combination of 2D operando imaging, 3D in situ tomography, and operando XRD and XAS provide new insight into the effect of the active/inactive mixed phases on the mechanical stability of the $Ge_{0.9}Se_{0.1}$ electrode.

2. Results and Discussion

In this study, operando 2D TXM image acquisition was implemented to monitor the dynamic morphological change of Ge and $Ge_{0.9}Se_{0.1}$ electrodes under galvanostatic operation. Ge and $Ge_{0.9}Se_{0.1}$ electrodes were (de)lithiated at approximately 0.2 C (1 μA for Ge and 0.6 μA for $Ge_{0.9}Se_{0.1}$). TXM images were recorded every 10 min during the first cycle. Fig. 1a,b shows the dynamic change of one Ge particle and one $Ge_{0.9}Se_{0.1}$ particle (around 3.5 μm volume equivalent shape diameter (VESD) for both) during the first lithiation. Fig. 1c,d shows the voltage profiles of the cycling process of the Ge and $Ge_{0.9}Se_{0.1}$ electrodes, as well as the dynamic optical density (OD) changes of the two active particles shown in Fig. 1a,b, as well as another Ge particle (5.3 μmin VESD in its pristine condition) and $Ge_{0.9}Se_{0.1}$ particle (3.2 μm in VESD in its pristine condition). Fig. S2a represents the Ge electrode microstructure in the pristine state. The dynamic change includes volume and OD changes of the active particles, and electrode cluster changes

during the cell operation. Fig. S2b shows the operando dynamic changes of the 5.3 μm Ge particle during the first lithiation (2.62 V ~ 0.01 V) and delithiation (0.13 V ~ 1.5 V) processes. The green outline around the particle at 2.62 V (pristine state) is replicated in the TXM images that were obtained during the lithiation process. The red outlines indicate the boundary of the particle at 0.01 V (lithiated condition). In the TXM images, OD (or pixel intensity) is directly related to the change of particle electron density[17], which can be used to detect the chemical phase changes (α-Li_xGe) of the particle. As shown in Fig. 1c there are negligible OD changes for the Ge particle for 100 min of the first lithiation until the operating voltage reached 0.31 V, which is in accordance with the results shown in Ref[17]. The capacity result in Ref[17] indicates that approximately one Li-ion has been inserted per Ge atom at this potential. If this is the case, it is possible that the OD changes for insertion of a single Li atom are below the detection limit of the TXM[17]. It is also possible that the Li-Ge alloy has a similar absorbance as pristine Ge. In addition, some of the Li ions could be consumed to form the SEI layer or lithiated into the carbon additive, leading to less than one Li atom inserted per Ge atom. At 0.28 V, the particle clearly shows an OD drop and volume expansion by Li-ion incorporation and phase change. Fig. 1c and Fig. S2b also demonstrate the shrinking of the particle and increase of the OD during the first delithiation. At the end of the delithiation (1.5 V), the OD and the overall size of the Ge particle did not return to the pristine condition. As shown in Fig. 1c, the delithiation capacity of the cell is approximately 50% of the lithiation capacity. Thus, the particle might have lost the electrical connection with the electrode as mentioned in Ref[17]. Another potential reason is nanopore formation in the Ge particle during the first delithiation[5, 23]. Fig. S2c shows an aggregated Ge particle cluster in the pristine (2.62 V), lithiated (0.01V), and delithiated (1.5 V) states. It clearly shows that the cluster expanded during lithiation and shrunk during delithiation.

The change of the cluster indicates the carbon-binder matrix changes because of the large volume change of the active particles. These morphological changes of the carbon-binder matrix can lead to the loss of the electrical connection of the active materials.

As compared with the dynamic change of the larger Ge particle (5.3 μm in VESD) shown in Fig. S2b, the smaller Ge particle exhibits a very similar dynamic change as shown in Fig. 1a,c. However, if we compare the dynamic changes of the Ge and $Ge_{0.9}Se_{0.1}$ particles, they have different dynamic changes. Fig. 1b,d demonstrates the $Ge_{0.9}Se_{0.1}$ particle experienced a sudden expansion and OD decrease between 4 h and 4.5 h. The Ge particle displays a relatively smooth expansion and slow OD decrease through the whole lithiation process, though there is still a larger change between 2 and 2.5 h. This phenomenon can be explained by the formation of a heterogeneous network of nm-sized crystalline Ge clusters, surrounded by the network of an amorphous super-ionically conductive inactive phase (Li-Se-Ge) as proposed by Klavetter et al.[10]. They have demonstrated an amorphous phase in a $Ge_{0.9}Se_{0.1}$ particle by employing High-resolution transmission electron microscopy (HRTEM)[10]. In addition, Fig. 1d shows a small decrease in the OD for both of the $Ge_{0.9}Se_{0.1}$ particles at the very beginning around 1 h that corresponds with a small voltage plateau near 1 V. This plateau has been attributed to the formation of Li-Se-Ge[10] and the slight OD decrease is due to the slight volume increase from this reaction as well as the impact on the absorbance caused by the Li-Se-Ge phase. The superconductive Li-Se-Ge network provides fast Li-ion pathways into the core of the $Ge_{0.9}Se_{0.1}$ particle because of its high ionic conductivity, which may lead to more uniform Li-ion incorporation into the $Ge_{0.9}Se_{0.1}$ particle than the Ge particle. The operando 2D TXM imaging results support the hypothesis of a super-ionically conductive Li-Se-Ge network formed in the

$Ge_{0.9}Se_{0.1}$ particle during the first lithiation process. The more sudden dynamic change of the $Ge_{0.9}Se_{0.1}$ particle is attributed to the effect of the Li-Se-Ge network. The encapsulating Li-Se-Ge layer around the nm-sized Ge particles can help them hold the original shape until the balance is broken, therefore, a more sudden change happens in $Ge_{0.9}Se_{0.1}$ particles.

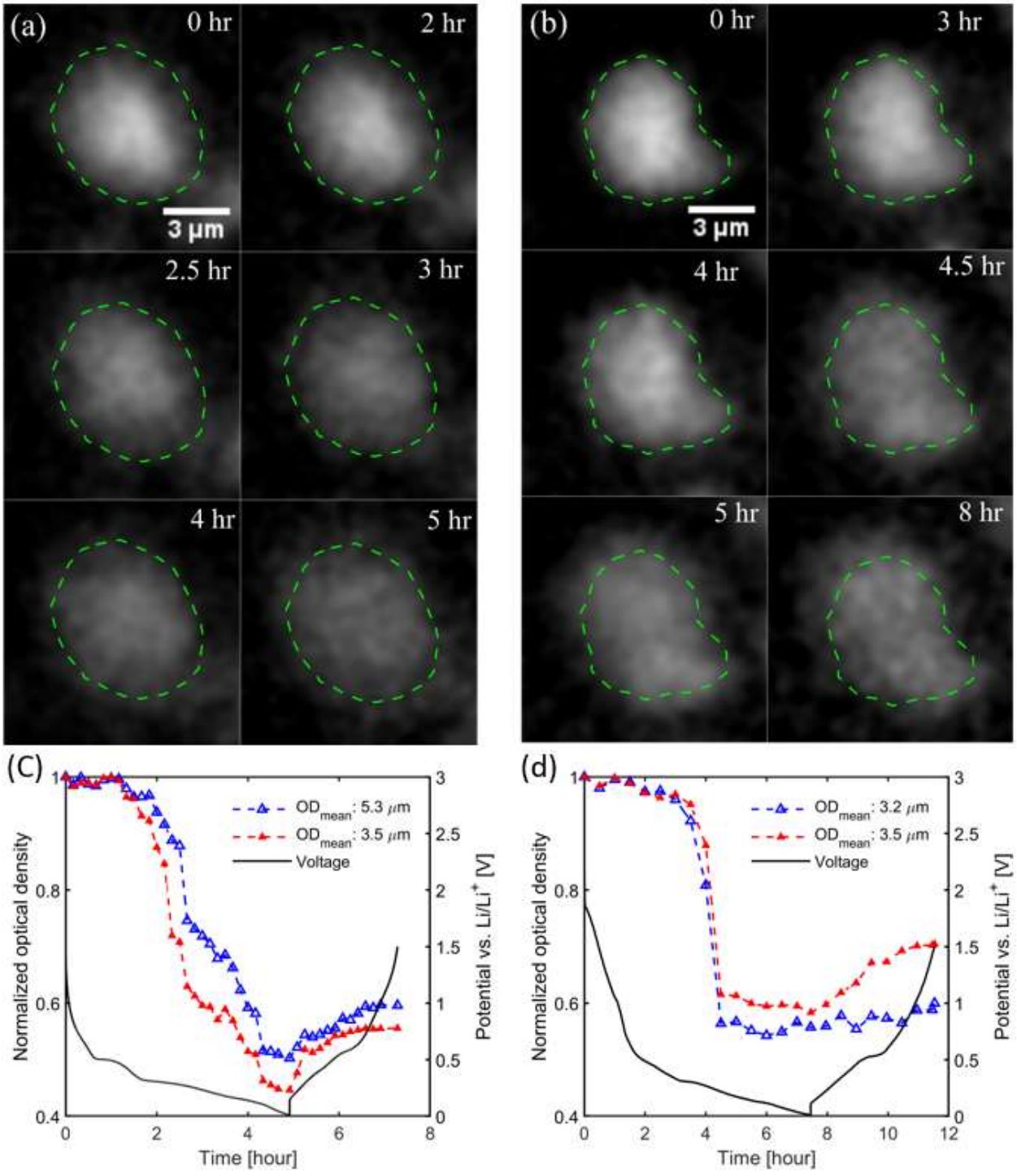

Fig. 1 Operando TXM. TXM dynamic images of (a) Ge and (b) $Ge_{0.9}Se_{0.1}$ particles (both around 3.5 μm in VESD) during the first lithiation. Normalized optical density (OD) dynamics of (c) Ge (5.3 μm and 3.5 μm in VESD) and (d) $Ge_{0.9}Se_{0.1}$ (3.5 μm and 3.2 μm in VESD) particles during

the first (de)lithiation. The OD data points were normalized by the average OD of the particles in their pristine states. The standard error is small (less than 0.5%) for all OD data points and the error bar is not shown in the plots. The $Ge_{0.9}Se_{0.1}$ TXM images were captured every 30 min under 0.6 μA of the constant current condition.

In situ tomography was implemented to obtain the 3D morphology of Ge and $Ge_{0.9}Se_{0.1}$ electrode structures of the in situ battery cells in their pristine, lithiated, and delithiated states. The tomographic images of the Ge or $Ge_{0.9}Se_{0.1}$ electrodes contained approximately 50 active particles. Fig. S3a-c displays the 3D morphological information of the 5.3 μm Ge particle displayed in Fig. S2b. The 3D morphologies of pristine, lithiated, and delithiated states are color mapped with mean curvature in the left top corners of the figures. The size of the particle in the pristine state is 5.3 μm in VESD and the surface area is 97.7 μm^2. The VESD is increased to 7.5 μm, which means a 283% volume expansion was achieved, and the surface area increased to 212 μm^2 via Li-ion incorporation. During the first delithiation, the particle shrinks to 208% in volume and 168% in the surface area of the pristine condition. Fig. S3d shows histograms of normalized X-ray attenuation coefficients in the pristine, lithiated, and delithiated states. The low intensity of the delithiated particle could be due to the incomplete delithiation and/or the formation of nanopores. To investigate the surface properties, the probability density of the minimum (κ_1) and maximum (κ_2) principal curvatures are demonstrated as interfacial shape distributions (ISD)[15, 24] in Fig. S3a-c. Compared with the pristine state, the lithiated particle shows a significant increase of the large curvatures and concave regions (R4, both κ_1 and κ_2 are negative). Region 4 in Fig. S3a indicates the portion (2.3%) of the concave area of the pristine particle. The concave area increased to 6.8% after the lithiation process and decreased to 5.1% after delithiation. The

rougher surface and increased concave area are caused by the inhomogeneous volume expansion of the pristine Ge particle.

Fig. 2 shows 3D morphological changes and curvature information of a Ge particle and a $Ge_{0.9}Se_{0.1}$ particle with similar size in the pristine, lithiated, and delithiated states. The pristine Ge particle is 2.7 μm and the pristine $Ge_{0.9}Se_{0.1}$ particle is 2.6 μm in VESD. For the Ge particle, the volume change is 223% after lithiation and 159% after delithiation. Similarly, the volume change is 251% after lithiation and 141% after delithiation for the $Ge_{0.9}Se_{0.1}$ particle. However, the curvature distribution shows very different surface properties. The $Ge_{0.9}Se_{0.1}$ particle shows a smoother surface and more homogeneous morphological change during (de)lithiation processes than the Ge particle, especially after delithiation (Fig. 2f). Klavetter et al. have demonstrated this phenomenon by employing HRTEM to show that $Ge_{0.9}Se_{0.1}$ particles do not experience nano-pore formation and have smoother surfaces during cycling[10]. The difference is attributed to the more homogeneous Li-ion transport in the $Ge_{0.9}Se_{0.1}$ particle due to the super-ionically conductive Li-Se-Ge network.

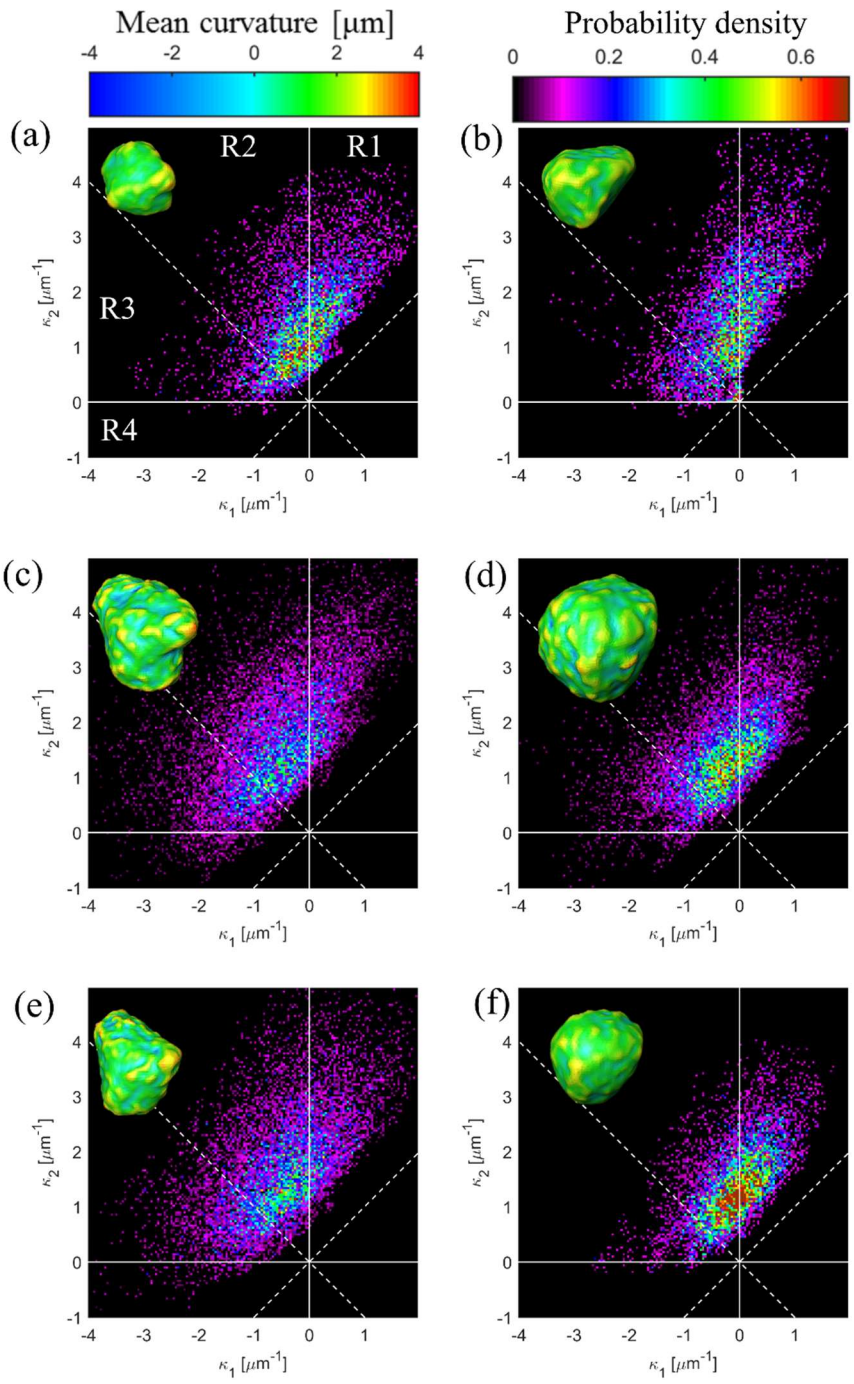

Fig. 2 In situ TXM tomography. Mean and principal curvature distributions of (a) pristine Ge particle (2.7 μm in VESD), (b) pristine $Ge_{0.9}Se_{0.1}$ particle (2.6 μm in VESD), (c) lithiated Ge particle, (d) lithiated $Ge_{0.9}Se_{0.1}$ particle, (e) delithiated Ge particle, and (f) delithiated $Ge_{0.9}Se_{0.1}$ particle.

To further explain the formation of the super-ionically conductive Li-Se-Ge network and its effect on the electrochemical performance, operando XRD measurements for Ge and $Ge_{0.9}Se_{0.1}$ cells during 0.1 C cycling was conducted at beamline 11-ID-C of the APS to investigate the dynamic phase changes. As shown in Fig. 3a-c, the XRD results for the pure Ge electrode show similar behavior to that reported in Ref[22]. We observed the disappearance of Ge peaks after 7 h and the formation of $Li_{15}Ge_4$ as the only crystalline product at the end of the first lithiation process. The crystalline $Li_{15}Ge_4$ phase disappeared during the process of delithiation and no crystalline Ge was observed at the end of delithiation. As shown in Fig. 3d-f, the peaks for crystalline GeSe and crystalline Ge are in their pristine states. During the process of lithiation, we observed the disappearance of GeSe peaks at the very beginning when the voltage reached its first plateau around 1 V. After that, the $Ge_{0.9}Se_{0.1}$ electrode did not regain the GeSe peaks during the first cycle. The disappearance of crystalline GeSe has been proposed to be due to the formation of the Li-Se-Ge inactive phase which corresponds to the observation of an OD decrease at about 1 V as shown in Fig. 1d. The crystalline Ge peaks started to disappear at about 10 h and no $Li_{15}Ge_4$ or other crystalline Li_xGe alloys were observed at the end of lithiation. This behavior represents a significant difference between pure Ge and $Ge_{0.9}Se_{0.1}$. As proposed by Ref [25], the formation of a crystalline $Li_{15}Ge_4$ phase from amorphous Li_xGe phases would require not only Ge−Ge bond breakage but also the rearrangement of Ge atoms (Ge migration), which involves a large activation barrier. We believe that the Li-Se-Ge network could add a large barrier to the rearrangement of Ge and suppress the formation of crystalline $Li_{15}Ge_4$. At the end of the first delithiation, no crystalline Ge was observed. We believe that the phase change of the $Ge_{0.9}Se_{0.1}$ electrode in the cycling process is between amorphous Ge and amorphous Li_xGe and

no crystalline phases are involved after the first cycle, which could be one of the mechanisms leading to the better mechanical stability of the $Ge_{0.9}Se_{0.1}$ electrode.

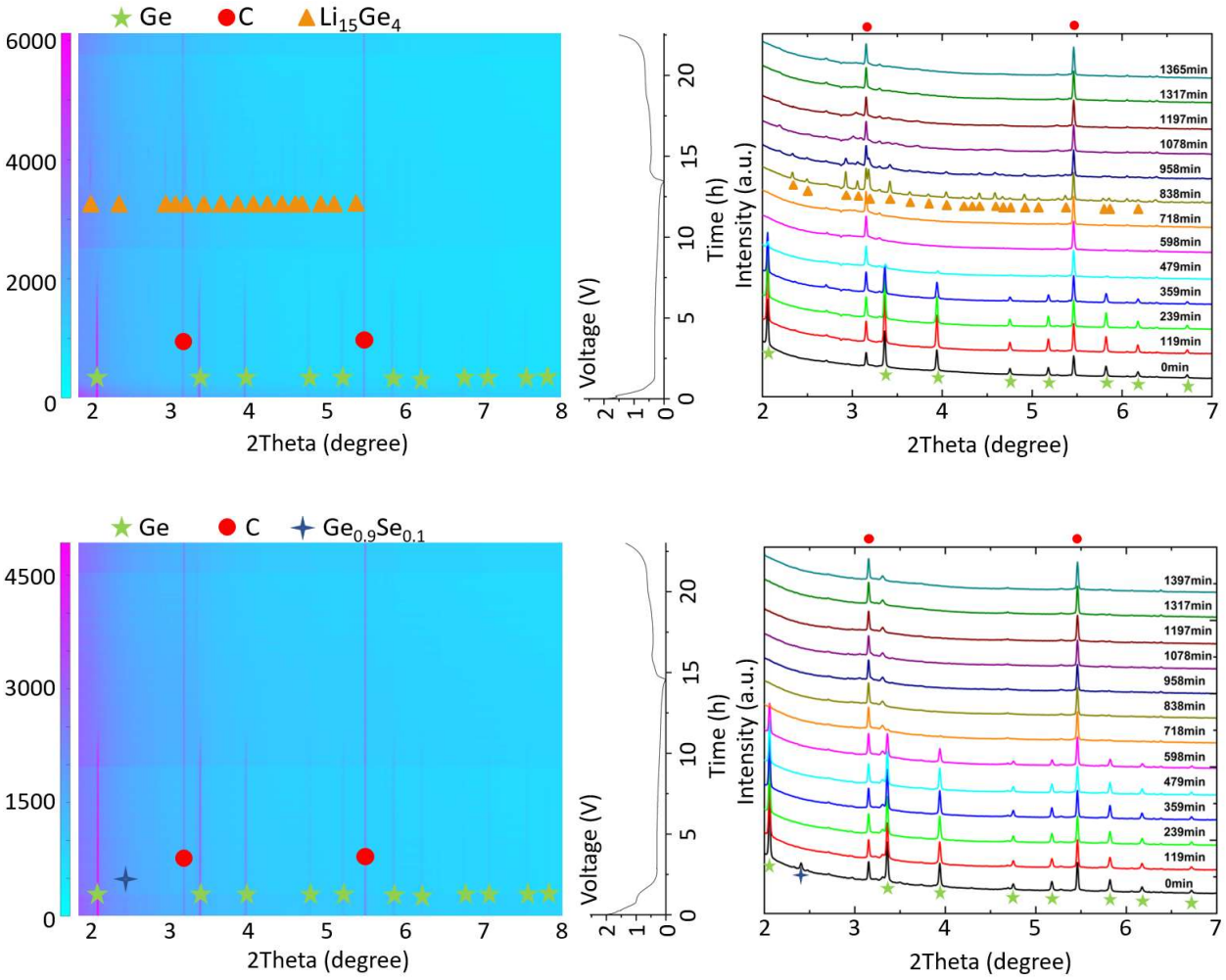

Fig. 3 Operando XRD results. (a) XRD patterns of a Ge cell during the first cycle at 0.1 C. (b) Voltage profile of the Ge cell. (c) Selected XRD patterns of the Ge cell. (d) XRD patterns of a $Ge_{0.9}Se_{0.1}$ cell during the first cycle at 0.1 C. (e) Voltage profile of the $Ge_{0.9}Se_{0.1}$ cell. (f) Selected XRD patterns of the $Ge_{0.9}Se_{0.1}$ cell. Lithium diffraction patterns have been marked off via Fit2D.

In order to obtain further insights into the amorphous Li-Se-Ge network in the $Ge_{0.9}Se_{0.1}$ electrode, operando X-ray absorption spectroscopy (XAS) of Ge K-edge and Se K-edge measurements during 0.1 C cycling was conducted at beamline 20-BM of the APS. The voltage profile of the operando coin cell is shown in Fig. 4a. The Se K-edge absorption energy for pristine $Ge_{0.9}Se_{0.1}$ matched well with the selenium standard (12658 eV) which is assigned to the transition of Se 1s core electrons to the unoccupied 4p state as displayed in Fig. 4b. The lack of data between 10 min and 178 min was due to an unexpected beamline outage at the APS. The X-ray absorption near edge spectroscopy (XANES) of Se clearly shows the energy shift to higher energy due to the increased oxidation state[26]. The standard K-edge shift for Li_2Se is 12660 eV as reported in Ref[27], which demonstrates a ratio of two Li ions per Se atom. The smaller energy shift of Se K-edge (12659 eV) in this experiment indicates that the oxidation state of Se is not Li_2Se. It accords with the operando XRD result shown in Fig. 3b, which did not show the crystalline Li_2Se phase during the lithiation process. The combination of XAS and XRD results demonstrate the formation of a Li-Se-Ge phase at the very beginning of the lithiation process. The Li-Se-Ge phase has been further proven to be inactive via the operando XAS results. As shown in Fig. 4b, once the Li-Se-Ge phase formed, its X-ray absorption remains the same during the entire cycling process as its white line does not shift from 12663 eV after initial lithiation, while the standard white line positions of Se and Li_2Se are 12660 eV and 12665 eV, respectively. Fig. 4c shows the comparison of the XANES spectra at the Ge K-edge between ex situ pure Ge and operando $Ge_{0.9}Se_{0.1}$ electrodes in the fully lithiated state. Both of their pristine states have similar spectra, but their spectra after lithiation are different. The spectrum for Ge after lithiation shows the formation of $Li_{15}Ge_4$ while the spectrum for $Ge_{0.9}Se_{0.1}$ indicates it formed an

amorphous Li_xGe phase. The corresponding normalized first derivatives of XANES (Fig. 4c) spectra are shown in Fig. S4, which clearly demonstrate the difference.

The operando XANES of the $Ge_{0.9}Se_{0.1}$ electrode and its first-derivative are shown in Fig. 4d,e. The Fourier Transforms (FT) of the extended X-ray absorption fine structure (EXAFS) spectra of the $Ge_{0.9}Se_{0.1}$ electrode during lithiation and delithiation processes are shown in Fig. 4f. Compared with the previous operando XAS data of the pure Ge electrode shown in Ref [19, 21, 22], Fig. 4d-f exhibits several different characteristics, which can be attributed to the Li-Se-Ge network. First, there is a clear Ge oxidation state change from 5 min to 173 min as shown in Fig. 4d with a decrease in X-ray absorption at the beginning. Fig. 4e also shows the first derivative peak shifts to a lower energy during this period. Both characteristics indicate a change of oxidation state. Interestingly, there is no clear change between 173 min and 275 min after the initial change in both XANES spectra and its first derivative which is similar to the pure Ge XANES result at the beginning of the first lithiation process [22]. This phenomenon indicates that Ge is involved in the reaction between Se and Li at the beginning of the lithiation process and an amorphous Li-Se-Ge network is formed. After the formation of the Li-Se-Ge network, the XANES spectra of the $Ge_{0.9}Se_{0.1}$ electrode behaved almost the same as the pure Ge electrode [19, 21, 22] because the reaction at this point is between Ge and Li. The spectra remain unchanged for some time, then the XANES spectra start to broaden and the first derivative peak starts to shift to lower energy at 309 min. These changes indicate the amorphization of Ge and the formation of amorphous Li_xGe phases. Second, the XANES spectra do not show the formation of crystalline $Li_{15}Ge_4$. As shown in Fig. 4c, at the end of lithiation, the XANES spectrum of Ge is in the transition between Ge and $Li_{15}Ge_4$ with no peak at 11113 eV, which indicates that only

amorphous Li_xGe phases are present at the end of lithiation. In addition, the first derivative spectra do not show a dramatic line shape change at the end of lithiation and the beginning of delithiation in Fig. 4e, which also indicates that there is no phase transformation between amorphous Li_xGe and crystalline $Li_{15}Ge_4$. The Fourier Transform of the EXAFS spectra were investigated to better understand the reaction mechanism that occurs during the electrochemical cycling. It can be observed in Fig. 4f that the magnitude of the first, second, and third shell decreased as lithiation proceeded. However, the first and second Ge-Ge shells are preserved and only the third Ge-Ge shell disappeared at the end of lithiation, which is different from the pure Ge data (The intensity of all three shells decreased at the end of lithiation reported by Lim et al.[22]). This result indicates insufficient Ge migration for the formation of crystalline $Li_{15}Ge_4$. Upon delithiation, the third shell did not recover and the intensity of the other two shells undergoes almost no change, which indicates that the phase transformation during delithiation is between amorphous Li_xGe and amorphous Ge.

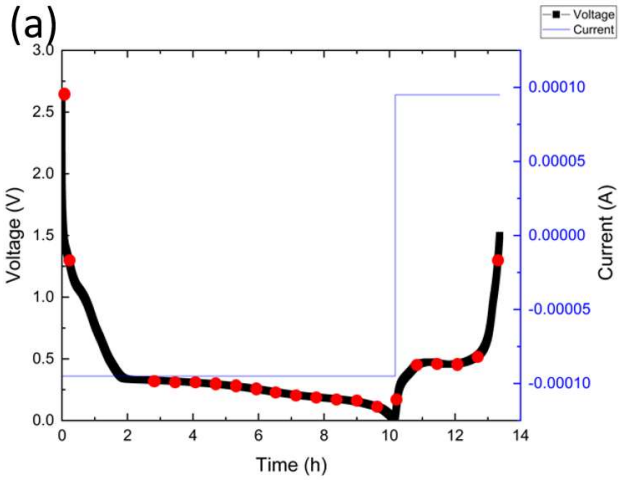
(a)
Voltage
Current
Voltage (V)
Current (A)
Time (h)

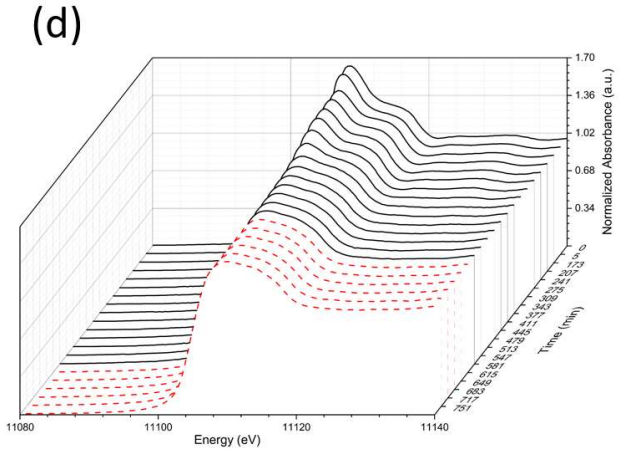
(d)
Normalized Absorbance (a.u.)
Time (min)
Energy (eV)

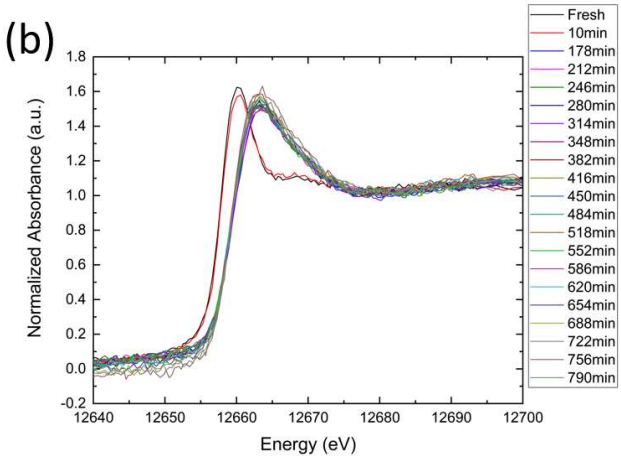
(b)
Fresh
10min
178min
212min
246min
280min
314min
348min
382min
416min
450min
484min
518min
552min
586min
620min
654min
688min
722min
756min
790min
Normalized Absorbance (a.u.)
Energy (eV)

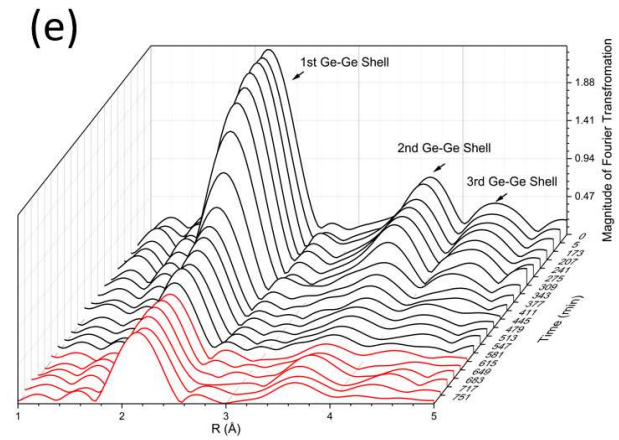
(e)
1st Ge-Ge Shell
2nd Ge-Ge Shell
3rd Ge-Ge Shell
Magnitude of Fourier Transfromation
Time (min)
R (Å)

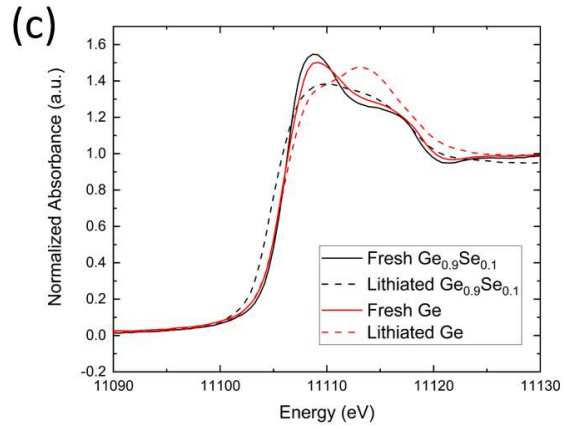
(c)
Fresh Ge0.9Se0.1
Lithiated Ge0.9Se0.1
Fresh Ge
Lithiated Ge
Normalized Absorbance (a.u.)
Energy (eV)

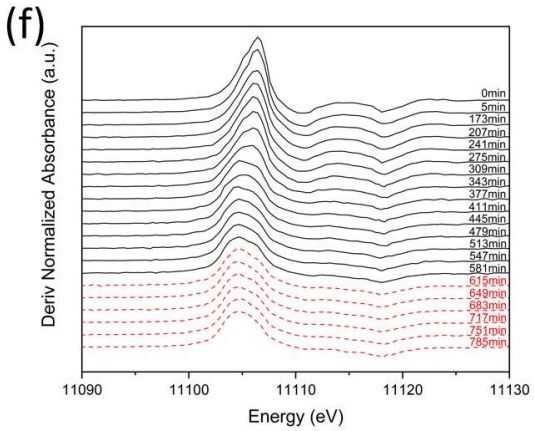
(f)
0min
5min
173min
207min
241min
275min
309min
343min
377min
411min
445min
479min
513min
547min
581min
615min
649min
683min
717min
751min
785min
Deriv Normalized Absorbance (a.u.)
Energy (eV)

Fig. 4 Operando XAS results for $Ge_{0.9}Se_{0.1}$. (a) Voltage and current profiles of a $Ge_{0.9}Se_{0.1}$ cell with highlighted data collecting points. (b) Selected selenium XANES results. (c) Comparison of ex situ Ge (red) and operando $Ge_{0.9}Se_{0.1}$ (black) electrodes in pristine (solid) and lithiated states (dash). (d) Selected germanium XANES results during lithiation (black solid) and delithiation (red dash). (e) The corresponding normalized first derivative of XANES spectra in (d). (f) Fourier Transforms of EXAFS spectra in (d) during lithiation (black) and delithiation (red).

3. Conclusion

In summary, the morphological evolution of Ge and $Ge_{0.9}Se_{0.1}$ electrodes has been investigated by using high resolution synchrotron TXM. An in situ battery cell was developed for the combined 2D operando TXM imaging and 3D in situ tomography. Unlike pure Ge, the observed 2D dynamic change of $Ge_{0.9}Se_{0.1}$ particles shows sudden morphological and OD changes during the first lithiation. Moreover, compared to the Ge particle, the $Ge_{0.9}Se_{0.1}$ particle has a more homogeneous volume change and smoother surface, which results in better mechanical stability for the $Ge_{0.9}Se_{0.1}$ electrode during cycling. The more sudden and homogeneous volume changes in the $Ge_{0.9}Se_{0.1}$ particles are attributed to the super-ionically conductive Li-Se-Ge network, which contributes to the fast ion transport into the particle as well as buffering the volume change. To verify the formation of the Li-Se-Ge network, operando XRD and XAS experiments were conducted. The results prove several hypotheses regarding the good cycling performance and rate capability of the $Ge_{0.9}Se_{0.1}$ electrode. A super-ionically conductive Li-Se-Ge network was formed at the beginning of the lithiation process and it is inactive during subsequent cycles. The formation of a crystalline $Li_{15}Ge_4$ phase was suppressed due to the encapsulation of the nm-sized Ge particles by the Li-Se-Ge network. This fundamental study brings some insights into

the design of high capacity LIB electrode materials. An in situ formed, super-ionically conductive, and inactive network in μm-sized active material particles could improve the mechanical stability of the electrode and lead to good cycling performance and rate capability.

4. Experimental Section

Design of the in situ TXM battery cell: An in situ battery cell was designed to monitor morphological changes of LIB electrodes by employing synchrotron TXM. For the in situ 3D TXM tomography and operando 2D TXM, the cell has to satisfy the following requirements; 1) no obstacles for blocking X-rays through all directions of the targeted material, 2) the targeted material absorbs sufficient amounts of X-rays to be distinguished from the background, 3) non-targeted components (cell housing, current collector, and electrolyte) are required to have less X-ray absorption through all directions, 4) the battery cell works properly under a high energy X-ray exposure on the TXM stage. Fig. S5a depicts a schematic of the in situ battery cell used for these experiments. For TXM capturing, a 5 μm thick working electrode (Ge or $Ge_{0.9}Se_{0.1}$) is coated on a carbon wire (Diameter = 30 μm) which is enclosed in the liquid electrolyte with a thin quartz capillary housing (Diameter = 500 μm, wall thickness = 10 μm). The electrochemical performance of the cell is measured by connecting two wires, one from the targeted electrode and one from a Li reference electrode, to an external instrument. Fig. S5d shows X-ray transmission rates of the cell components at varying photon energy. The X-ray transmission rate of Ge dramatically drops above 11.1 keV of photon energy by exceeding the K-shell absorption edge. At an 11.2 keV photon energy, μm-sized Ge particles absorbed 30% - 60% of the irradiated X-rays while around 30% of the X-rays are absorbed in the quartz glass housing and ethylene carbonate (EC)/diethyl carbonate (DEC) electrolyte. As shown in Fig. S5c, Ge particles

are clearly identified by their brighter color compared to the background because of their high attenuation.

Fabrication of Ge and $Ge_{0.9}Se_{0.1}$ electrodes for in situ TXM: The electrode slurry was composed of 50 wt% active material (Ge or $Ge_{0.9}Se_{0.1}$), 30 wt% super-P carbon black conductive additive, and 20 wt% carboxymethyl cellulose (CMC) polymer binder from 5% CMC solution. The CMC binder (90 kDa, Sigma-Aldrich, St. Louis, MO, USA) was pre-dissolved in deionized water. µm-sized Ge and $Ge_{0.9}Se_{0.1}$ powders were synthesized as described in Ref[10] and the super-P carbon black (C65) was purchased from TIMCAL. A carbon wire (Diameter = 30 µm, WPI, Sarasota, FL, USA) was selected as the current collector for the working electrode because it has a high X-ray transmission rate and is more rigid in the electrolyte-filled cell. One end of the carbon wire (bottom side) was attached to a nickel alloy wire (Diameter = 75 µm, Alfa Aesar, Reston, VA, USA) in a 1 cm length of fused silica tubing (Diameter = 250 µm, SGE, Australia). The long nickel alloy wire is connected to an external circuit. The two open ends of the silica capillary were sealed with epoxy. In an oxygen plasma chamber (PE-50, Plasma Etch, Carson City, NV, USA), the carbon wire was etched for 2 min to enhance surface adhesion with the electrode slurry. The surface-treated carbon wire set was laid on a copper sheet and uniformly coated with the electrode slurry via a film casting doctor blade. The wire electrode was separated from the copper sheet when the electrode slurry was partially dried to maintain uniform thickness through the carbon wire. Then, it was dried in a vacuum oven at 110 °C for 10 h. An SEM image of the fabricated Ge electrode is shown in Fig. S5b.

Assembly of the in situ battery cell for TXM: The in situ battery cell was assembled in an argon-filled glovebox (under O_2 < 0.1 ppm, H_2O < 0.1 ppm; Unilab 2000, Mbraun, Stratham, NH, USA). A small piece of Li metal (thickness of 0.6 mm foil, Sigma-Aldrich, St. Louis, MO, USA) was attached on the copper wire (D=200 μm) as the reference electrode. The reference electrode was attached to the silica capillary wall by epoxy. The silica capillary prevents direct contact between the working and reference electrodes. The entire set of electrodes was carefully inserted into a funnel-shaped open end (Dia = 3 mm) of a quartz capillary (Hampton, Aliso Viejo, CA, USA) and the working electrode was located in the thin capillary region (inner diameter = 500 μm, wall thickness = 10 μm). To mount the electrode on the cell housing, 0.02 ml of PDMS mixture (Sylgard 184, Dow Corning, Auburn, MI, USA) was injected into the funnel-shaped end and cured at 80 °C on a hotplate for 15 min (PDMS electrode substrate in Fig. S5a). The quartz housing was fully filled with 1 M $LiPF_6$ EC/DEC (1:1 v/v) electrolyte through a micro-syringe. The PDMS seal was capable of being penetrated by the micro-syringe and preventing leaking of the electrolyte. After injecting electrolyte, the top, open-end of the capillary was sealed with 5-min epoxy. Both ends of the quartz capillary were sealed with torr epoxy (Torr seal vacuum epoxy, Agilent Technologies, Lexington, MA, USA) to prevent leaking of the electrolyte. The nickel alloy wire of the working electrode and the copper wire of the reference electrode were connected to a battery cycler (BT 2000, Arbin, College Station, TX, USA) during the operando TXM study.

Combined in situ TXM tomography and operando TXM imaging: In situ battery cells were assembled as described above to investigate morphological changes of the Ge and $Ge_{0.9}Se_{0.1}$ electrodes by employing in situ TXM tomography and operando TXM imaging. Here, the in situ

tomography gives a 3D scan of a targeted electrode by capturing TXM images at 720 angles over a 180° rotation when the battery cell is not working. To avoid the hard X-ray induced damage on the carbon-binder matrix, intermittent X-ray exposure during image capturing was used, as shown in Ref [28]. The operando TXM imaging periodically records a series of TXM images for the targeted electrode during cell operation. The experimental procedure was as follows: 1) in situ tomography for a pristine electrode, 2) operando TXM imaging during the first lithiation of the pristine electrode, 3) in situ tomography for the lithiated electrode, 4) operando TXM imaging during the first delithiation of the lithiated electrode, and 5) in situ tomography for the delithiated electrode. The TXM images with a 38.8 nm pixel size were recorded with 1 s exposure time. The in situ battery cells were operated at 0.1 - 0.2 C rates under galvanostatic conditions.

Operando coin cells assembly: Ge and $Ge_{0.9}Se_{0.1}$ electrodes for XRD and XAS were fabricated from an 80:10:10 (wt%) mixture of active material, carbon black, and polyvinylidene difluoride (PVDF). The mixture was added into n-methylpyrrolidone (NMP) solution and mixed for 20 h to homogenize. The produced slurries were coated onto a thin pyrolytic graphite sheet and a piece of copper foil for XRD and XAS, respectively. The graphite sheet was used as the current collector for XRD to avoid strong X-ray absorption during data collection. The electrodes were dried at 100 °C in a vacuum oven for 12 h. Circular discs of 1.11 cm diameter were punched out of the electrode film and stored in an argon-filled glove box for coin cell assembly. CR2032 coin cells were modified and used in this study. 2 mm diameter holes were punched in the center of both anode and cathode cases and 30 μm thick Kapton tape was adopted to seal the hole on both sides of the case. Fig. S6 displays the order of operando coin cell assembly. The current collector

on top of the anode case with a 2 mm hole was to maximize the contact of the electrode. The electrode was placed on the current collector and then 20 µL of $LiPF_6$ electrolyte was added. A Celgard 2400 separator was placed on top of the electrode with an additional 20 µL of electrolyte on top of it. A piece of lithium metal of 1.27 mm diameter was laid on the separator followed by a stainless-steel plate (with a 2 mm hole at the center) and a wave spring. The cell was crimped and taken out of the glove box for electrochemical evaluation.

Synchrotron X-ray diffraction: The operando XRD experiment was conducted at beamline 11-ID-C of the APS with a photon wavelength of 0.1174 Å and energy of 105.6 keV. The incident beam size on the sample was 50 µm * 50 µm. Measurements were carried out in transmission mode. The detector was located 1800 mm from the sample. The scattering intensity was detected on a 2D Perkin-Elmer detector with a pixel size of 200 µm (2048 * 2048 pixels). The schematic for the synchrotron XRD setup is shown in Fig. S7. Both the Ge and $Ge_{0.9}Se_{0.1}$ coin cells were cycled at a constant current rate of 0.1 C. The diffraction data were collected with a 10 min interval. The exposure time was 0.5 s and 40 captures were averaged for each data collection. The 2D diffraction patterns generated via operando XRD were calibrated using a standard CeO_2 sample and converted to 1D patterns via Fit2D software. Data were analyzed via Match! software.

Synchrotron X-ray absorption spectroscopy: Germanium and selenium K-edge XAS measurements were performed at beamline 20-BM of the APS. Energy calibration was monitored by the use of a Ge standard (11103.0 eV). The beam size employed in this study was

500 μm * 500 μm and the incident beam was monochromatized by using a Si (111) fixed-exit, double-crystal monochromator. The XAS spectra were recorded in transmission for the in situ coin cell with a 34 min interval using the same coin cell setup as in XRD (Fig. S6). The spectra were normalized via ATHENA software to obtain the X-ray absorption near edge structures (XANES) and extended X-ray absorption fine structure (EXAFS).

Conflicts of interest

There are no conficts to declare.

Acknowledgments

This work was supported by the US National Science Foundation under Grants No. 1603847, No. 1603491 and No. 1604104. CBM gratefully acknowledges support from the Robert A. Welch foundation through grant F-1436. We also used resources related to the Advanced Photon Source, a U.S. Department of Energy (DOE) Office of Science User Facility operated for the DOE Office of Science by Argonne National Laboratory under Contract No. DE-AC02-06CH11357.

References

1. J. Graetz, C. Ahn, R. Yazami and B. Fultz, *Journal of The Electrochemical Society*, 2004, **151**, A698-A702.
2. C.-Y. Chou and G. S. Hwang, *Journal of Power Sources*, 2014, **263**, 252-258.
3. C. K. Chan, H. Peng, G. Liu, K. McIlwrath, X. F. Zhang, R. A. Huggins and Y. Cui, *Nature nanotechnology*, 2008, **3**, 31-35.
4. T. Kennedy, E. Mullane, H. Geaney, M. Osiak, C. O'Dwyer and K. M. Ryan, *Nano letters*, 2014, **14**, 716-723.
5. X. H. Liu, S. Huang, S. T. Picraux, J. Li, T. Zhu and J. Y. Huang, *Nano Letters*, 2011, **11**, 3991-3997.
6. J. Liu, Y. Li, X. Huang, R. Ding, Y. Hu, J. Jiang and L. Liao, *Journal of Materials Chemistry*, 2009, **19**, 1859-1864.
7. J. Y. Huang, L. Zhong, C. M. Wang, J. P. Sullivan, W. Xu, L. Q. Zhang, S. X. Mao, N. S. Hudak, X. H. Liu and A. Subramanian, *Science*, 2010, **330**, 1515-1520.
8. H. X. Dang, K. C. Klavetter, M. L. Meyerson, A. Heller and C. B. Mullins, *Journal of Materials Chemistry A*, 2015, **3**, 13500-13506.
9. A. R. Kamali and D. J. Fray, *Rev. Adv. Mater. Sci*, 2011, **27**, 14-24.
10. K. C. Klavetter, J. P. De Souza, A. Heller and C. B. Mullins, *Journal of Materials Chemistry A*, 2015, **3**, 5829-5834.
11. K. J. Harry, D. T. Hallinan, D. Y. Parkinson, A. A. MacDowell and N. P. Balsara, *Nature Materials*, 2014, **13**, 69-73.
12. D. P. Finegan, M. Scheel, J. B. Robinson, B. Tjaden, I. Hunt, T. J. Mason, J. Millichamp, M. Di Michiel, G. J. Offer and G. Hinds, *Nature communications*, 2015, **6**.
13. M. Ebner, F. Marone, M. Stampanoni and V. Wood, *Science*, 2013, **342**, 716-720.
14. F. Sun, H. Markoetter, D. Zhou, S. S. S. Alrwashdeh, A. Hilger, N. Kardjilov, I. Manke and J. Banhart, *ChemSusChem*, 2016, **9**, 946-950.
15. J. Wang, Y. c. K. Chen-Wiegart and J. Wang, *Angewandte Chemie*, 2014, **126**, 4549-4553.
16. J. Wang, C. Eng, Y.-c. K. Chen-Wiegart and J. Wang, *Nature Communications*, 2015, **6**.
17. J. N. Weker, N. Liu, S. Misra, J. Andrews, Y. Cui and M. Toney, *Energy & Environmental Science*, 2014, **7**, 2771-2777.
18. T. Li, X. Zhou, Y. Cui, C. Lim, H. Kang, B. Yan, J. Wang, J. Wang, Y. Fu and L. Zhu, *Electrochimica Acta*, 2019, **314**, 212-218.
19. L. Y. Lim, S. Fan, H. H. Hng and M. F. Toney, *Advanced Energy Materials*, 2015, **5**, 1500599.
20. L. C. Loaiza, N. Louvain, B. Fraisse, A. Boulaoued, A. Iadecola, P. Johansson, L. Stievano, V. Seznec and L. Monconduit, *The Journal of Physical Chemistry C*, 2018, **122**, 3709-3718.
21. K. E. Silberstein, M. A. Lowe, B. Richards, J. Gao, T. Hanrath and H. D. Abruña, *Langmuir*, 2015, **31**, 2028-2035.
22. L. Y. Lim, N. Liu, Y. Cui and M. F. Toney, *Chemistry of Materials*, 2014, **26**, 3739-3746.
23. X. Zhou, T. Li, Y. Cui, M. L. Meyerson, C. B. Mullins, Y. Liu and L. Zhu, *ACS Applied Energy Materials*, 2019, 2, 2441-2446.
24. D. Kammer and P. W. Voorhees, *Acta Materialia*, 2006, **54**, 1549-1558.
25. W. Tang, Y. P. Liu, C. X. Peng, M. Y. Hu, X. C. Deng, M. Lin, J. Z. Hu and K. P. Loh, *Journal of the American Chemical Society*, 2015, **137**, 2600-2607.

26. C. Luo, Y. Xu, Y. Zhu, Y. Liu, S. Zheng, Y. Liu, A. Langrock and C. Wang, *ACS Nano*, 2013, **7**, 8003-8010.
27. G.-L. Xu, T. Ma, C.-J. Sun, C. Luo, L. Cheng, Y. Ren, S. M. Heald, C. Wang, L. Curtiss, J. Wen, D. J. Miller, T. Li, X. Zuo, V. Petkov, Z. Chen and K. Amine, *Nano Letters*, 2016, **16**, 2663-2673.
28. C. Lim, H. Kang, V. De Andrade, F. De Carlo and L. Zhu, *Journal of Synchrotron Radiation*, 2017, **24**, 695-698.